Superalloys 2008
Roger C. Reed, Kenneth A. Green, Pierre Caron, Timothy P. Gabb, Michael G. Fahrmann, Eric S. Huron and Shiela A. Woodard
TMS (The Minerals, Metals & Materials Society), 2008

GAMMA PRIME MORPHOLOGY AND CREEP PROPERTIES OF NICKEL BASE SUPERALLOYS WITH PLATINUM GROUP METAL ADDITIONS

J.S. Van Sluytman[1], A. Suzuki[2], A. Bolcavage[3], R.C. Helmink[3], D.L. Ballard[4], and T.M. Pollock[1]
[1] University of Michigan, Department of Materials Science Engineering, 2300 Hayward Street, Ann Arbor, MI 48109-2136, USA
[2] GE Global Research, One Research Cr., Niskayuna, NY 12309, USA
[3] Rolls Royce North American Technologies, Inc., 2001 South Tibbs Avenue, Indianapolis, IN 46241, USA
[4] Materials & Manufacturing Directorate, Air Force Research Laboratory, Wright-Patterson AFB, OH 45433, USA

Keywords: creep, platinum group metals, lattice misfit

Abstract

The microstructure and creep properties of platinum group metal (PGM) modified nickel based superalloys have been investigated. Alloys containing Pt and/or Ir along with variations in Cr, Ta, Re, Ru, and W exhibited relatively high solidus and liquidus temperatures. Differential thermal analysis (DTA) showed a strong dependence of the γ´ solvus on the level of Ta. The morphology of the γ´ precipitates was influenced by the presence of Cr, Ta, Ru, and W and ranged from cuboidal to semi-spherical. Compression creep tests were conducted at 1000°C at stresses ranging from 40-90 MPa. Alloys containing approximately 8 wt% Pt combined with Cr and Ta displayed the best resistance to creep deformation at stresses around 80 MPa. Post-creep analysis of the rafted structures indicated that all PGM modified alloys without Ru and W possessed positive misfit with magnitudes ranging from ≈ 0.3 to 1.5%. The partitioning of PGMs between the γ and γ´ phases and their resultant influence on creep performance is discussed.

Introduction

Nickel based superalloys for turbine blade applications require a combination of high oxidation resistance as well as high creep resistance [1, 2]. While ceramic thermal barrier coatings and intermetallic bond coats are employed with commercial superalloys to help mitigate high temperature environmental degradation [3, 4], high intrinsic oxidation resistance and mechanical strength is desirable in the event that these protective coatings fail. Platinum group metal (PGM) elements are well known for their tendency to inhibit oxidation of NiAl-based bond coats [5-8]. More recently γ - γ´ bond coats with high oxidation resistance have been demonstrated [9, 10]. Thus, PGM-containing γ - γ´ alloys could potentially be of interest either as bond coats or as bulk superalloys in applications where oxidation resistance is critical.

Mechanical properties of γ - γ´ microstructures are sensitive to precipitate size and morphology [2, 11] and are therefore sensitive to partitioning of elements to the phases as well. PGMs such as Pt, Ir, and Ru have atomic radii of 0.139, 0.136, and 0.134 nm, respectively. Since the radii are much larger than Ni (0.125 nm), additions of these elements may substantially change the lattice parameters of either the γ or γ´ phases or their resultant misfit depending on their partitioning behavior. Platinum (Pt) is known to preferentially partition to the $L1_2$ structure, occupying Ni sites [10, 12, 13]. Iridium (Ir) partitions near equally between γ and γ´, but may partition to a higher extent to either phase if elements such as Re, Cr, Ru, and/or W are present [14, 15]. Since additions of Cr, Ta, and Re are likely to be present in superalloys containing PGMs, the partitioning behavior of the PGM elements is likely to be complex. Alloys without high levels of refractory alloying additions often contain spherical precipitates [16] with misfit values in the range of 0 – 0.3%. However, most commercial turbine blade alloys contain cuboidal γ´ precipitates due to the strong partitioning of refractory elements such as Re [17]. The relationship between precipitate morphology, elemental partitioning and creep strength is not fully understood for PGM additions.

To date, research on the creep strength of nickel based superalloys containing PGMs has focused on Ru additions [18-25]. This is due to the fact that Ru-containing alloys are generally less susceptible to TCP formation, allowing the beneficial additions of solid solution strengthening elements, including Cr [26]. Additionally, among the PGMs, the least expensive element is Ru. There has been only limited investigation of Ir additions to Ni-base superalloys [27, 28]. Creep tests conducted at 900°C and 392 MPa on single crystals (such as TMS-173) with and without Ir showed improved service life with Ir additions. Creep properties of Pt-containing alloys are limited to one study on a Ni-base alloy containing approximately 10 wt% Pt with creep tests at 1000°C under a constant load of 103 MPa, where a relatively low creep rate of about 2.5 x 10^{-8} s^{-1} was observed [29]. However, this alloy was crept to rupture and information regarding its post-creep microstructure was not reported.

The aim of this research was to investigate the influence of PGMs on various polycrystalline Ni-base superalloys with modified amounts of PGM additions, specifically, Pt and/or Ir. Liquidus, solidus, and γ´ solvus temperatures were used to define optimal heat treatment conditions that produced stable γ/γ´ two-phase microstructures. Compression creep tests were conducted to measure minimum creep rates and to observe the directional

coarsening behavior of the PGM alloys. Additionally, microstructures prior to creep and post-creep were studied by TEM, and lattice misfit between the two phases was estimated based on the γ - γ′ interfacial dislocation networks. Oxidation studies on the same group of alloys are being conducted by Gleeson and co-workers and will be reported elsewhere.

Experimental

PGM modified Ni-base superalloy ingots 10mm in diameter with a varying length of 13-17mm were produced by vacuum arc-melting in facilities located at Iowa State University. A design of experiments (DOE) approach was employed to identify two consecutive matrices of alloys for investigation. The Phase I matrix had elemental variations of Cr, Re, and Ta with the additions of Pt and Ir. The Phase II matrix also considered additions of Ru and W. Alloys discussed within this paper are listed in Table 1.

DTA samples were electric discharge machined (EDM) into 3-4mm diameter cylinders weighing approximately 250-300 mg. DTA analysis was carried out using a Setaram SETSYS apparatus. A 0.999% pure Pt reference was used for all samples being tested. Samples were placed within an alumina crucible and experiments were conducted within an argon atmosphere. A scan rate of 5°C/min was used for all samples as this rate has been shown to produce an accurate determination of solidus and liquidus temperatures [30, 31].

Creep samples were sectioned 4mm x 4mm x 8mm in dimension by EDM. Compression creep tests were conducted using an OXY-GON creep furnace with a TZM alloy compression creep fixture. All tests were conducted at a constant temperature of 1000°C (1273K) ±2°C under a vacuum of ≈ 10^{-7} torr. Two type-R thermocouples were placed next to the specimen located within the heat zone to ensure accurate temperature measurements. Outside the heat zone, but still within the vacuum furnace, two LVDTs were used to measure creep strain. All tests were terminated after approximately 1% creep strain accumulated. At the end of each test, the sample remained loaded during cooling to room temperature to maintain the dislocation substructure [32].

Heat treatments were conducted within a standard cylindrical tube furnace. All samples were first encapsulated within quartz cylindrical tubes filled back with argon. DTA experiments were utilized to define solution and aging temperatures. Following solution heat treatments, samples were rapidly water quenched by shattering the glass capsule in water. The procedure for DOE Phase I and II alloys is as follows: Phase I: 1330°C / 6 hr. → Water Quench → 1050°C / 4 hr. → Air Cool; Phase II: (T_S -5)°C / 6 hr. → Water Quench → 1050°C / 4 hr. → Air Cool, where T_s denotes the solidus temperature.

Samples characterized by scanning electron microscopy (SEM) were mounted in bakelite, and subsequently polished up to 0.05 µm alumina micropolish. Samples were etched with a solution of 33% acetic acid ($C_2H_4O_2$), 33% deionized water, 33% nitric acid (HNO_3), and 1% hydrofluoric acid (HF). A Philips XL-30 FEG SEM was used to analyze microstructure in post heat treatment and post-creep conditions. All images were acquired in BSE mode with a voltage of 20 kV.

TEM foils were prepared by hand polishing samples sectioned parallel to the applied stress axis to approximately 0.1 mm thickness using grit paper. Thinning utilized twin jet electropolishing at a temperature of approximately -40°C. The solution used for all samples consisted of 68% methanol (CH_3OH), 10% percholoric acid ($HClO_4$), 9% distilled water, and 13% butyl cellosolve ($C_6H_{14}O_2$). TEM investigations were performed on a Philips CM-12 microscope with an accelerating voltage of 120 kV. The magnitude of the lattice misfit, δ, was estimated by analysis of interfacial dislocation spacings following small amounts of creep straining and is defined as:

$$\delta = \frac{|\vec{b}|}{d} \qquad \text{Eq.(1)}$$

where $\vec{b}$ is the Burgers vector and d is the interfacial dislocation spacing measured at γ - γ′ interfaces by the line intercept method.

Results

Table I lists the compositions and results of DTA analyses for all alloys investigated. As apparent from Table I, alloys containing only Ir as the PGM addition exhibit the highest average solidus temperatures (1365-1390°C), whereas those containing higher amounts of Pt have lower solidus temperatures (1345-1380°C). Alloys that do not contain Ta have γ′ solvus temperatures ranging from 1140-1170°C. Once Ta is added to the system by about 6 wt%, the γ′ solvus increases by approximately 200°C, leaving a window of approximately 20-40°C between the γ′ solvus and solidus temperatures. Figure 1 demonstrates the influence of elemental additions on solvus and solidus temperatures. Alloys in the figure were given similar heat treatments as stated in the

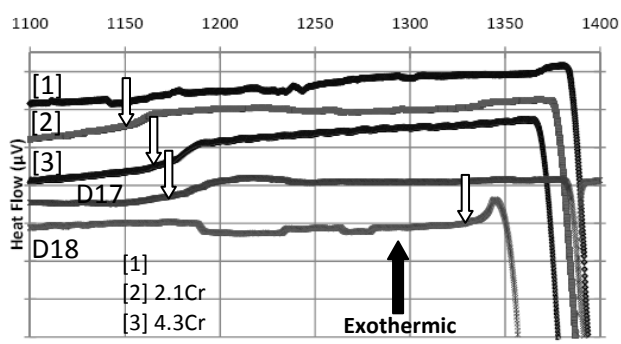

Figure 1: DTA of alloys containing higher amounts of Pt. Phase I alloys are listed by designated number. Alloy 1 contains (in wt%) ≈ 6.5Al-15.8Pt-0.3Hf. Alloys 2 and 3 contain same composition as alloy 1 with additional Cr amounts stated within the graph.

experimental section in reference to Phase I alloys. The white arrows indicate solvus temperatures, whereas the one black arrow indicates the exothermic direction. Increasing the amounts of Cr from alloy 1 to 2 to 3 increases the γ′ solvus temperature while decreasing the solidus temperature. Alloy D17 has the same composition of alloy 3 but with the addition of Re, which decreases the solvus mark while raising the solidus temperature to the point similar to alloy 1. Alloy D18, which is similar to alloy 3

Table I: Compositional profile of DOE Phase I & II alloys with associated DTA results post-heat treatments.

Phase I

PGM Additions	Composition (wt%)									DTA (°C)		
	Alloy	Al	Pt	Ir	Cr	Re	Ta		Hf	T_s (Solidus)	T_L (Liquidus)	γ′ Solvus
Ir	D1	6.8	0	8.1	2.2	0	6.1		0.3	1379	1398	1337
	D3	6.8	0	8.4	4.6	0	0		0.3	1387	1420	1143
	D4	6.7	0	7.9	4.3	3.1	6		0.3	1365	1406	1337
Pt	D5	6.8	8.2	0	2.2	0	6.1		0.3	1368	1398	1321
	D7	7	8.5	0	4.5	0	0		0.3	1373	1405	1153
	D8	6.7	8	0	4.3	3.1	5.9		0.3	1351	1398	1337
Ir-Pt	D10	6.3	7.6	7.5	2	2.9	5.6		0.3	1375	1417	1333
	D12	6.4	7.8	7.6	4.1	0	5.8		0.3	1363	1400	1336
	D13	6.6	7.9	7.8	4.2	3	0		0.3	1366	1407	1172
Higher Pt	D15	6.5	15.1	0	2	2.9	5.6		0.3	1362	1403	1341
	D17	6.4	15.5	0	4.1	0	5.7		0.3	1347	1383	1333
	D18	6.5	15.8	0	4.2	3	0		0.3	1383	1424	1152

Phase II

PGM Additions	Composition (wt%)										DTA (°C)		
	Alloy	Al	Pt	Ir	Cr	Re	Ta	Ru	W	Hf	T_S (Solidus)	T_L (Liquidus)	γ′ Solvus
Pt	D19	6.5	7.8	0	4.2	3	5.8	1.6	2.9	0.3	1353	1385	1268
	D22	6.3	7.6	0	4	2.9	5.6	3.1	5.7	0.3	1350	1386	1266
Ir-Pt	D24	6.1	7.4	5.8	3.9	2.8	5.5	1.5	5.6	0.3	1365	1404	1291
	D25	6.2	7.5	5.9	4	2.9	5.5	3.1	2.8	0.3	1364	1403	1290
Higher Pt	D27	6.1	14.8	0	3.9	2.8	5.5	1.5	2.8	0.3	1352	1385	1270

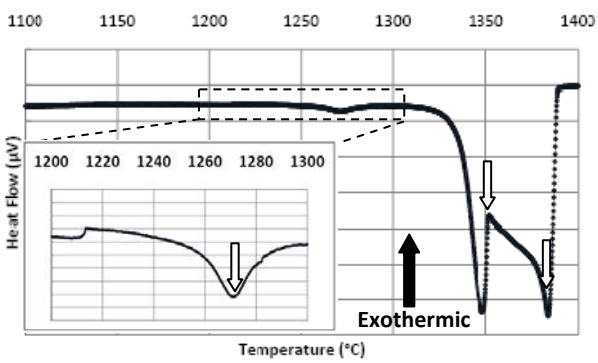

Figure 2: DTA of alloy D27 . The white arrows refer to the solvus, solidus, and liquidus marks.

but now with Ta, has a higher solvus, close to the solidus temperature, which is somewhat lowered by the Ta.

Figure 2 shows a DTA scan of alloy D27 from Phase II. The inset highlights the heat flow occurring between 1200 to 1300°C. From the inset, the γ′-solvus appears to be at 1270°C. Above 1270°C, however, there are two endothermic reactions. As stated in the experimental section, Phase II samples were homogenized approximately 5°C below the solidus temperature and SEM images (not shown here) indicated no eutectic regions but rather large (≈ 4 µm) γ′ particles which did not fully solutionize. As will be discussed later, this is due to the presence of a strongly bimodal precipitate structure. At 1329°C, incipient melting begins and the liquidus temperature is at 1385°C. All alloys from Phase II displayed profiles similar to Figure 2.

Microstructure

Figure 3 displays how various elemental additions change the morphological characteristics of the γ′ precipitates. All samples shown in Figure 3 were placed within the SEM chamber simultaneously and were imaged using the same brightness/contrast values in BSE mode. Images that appear to

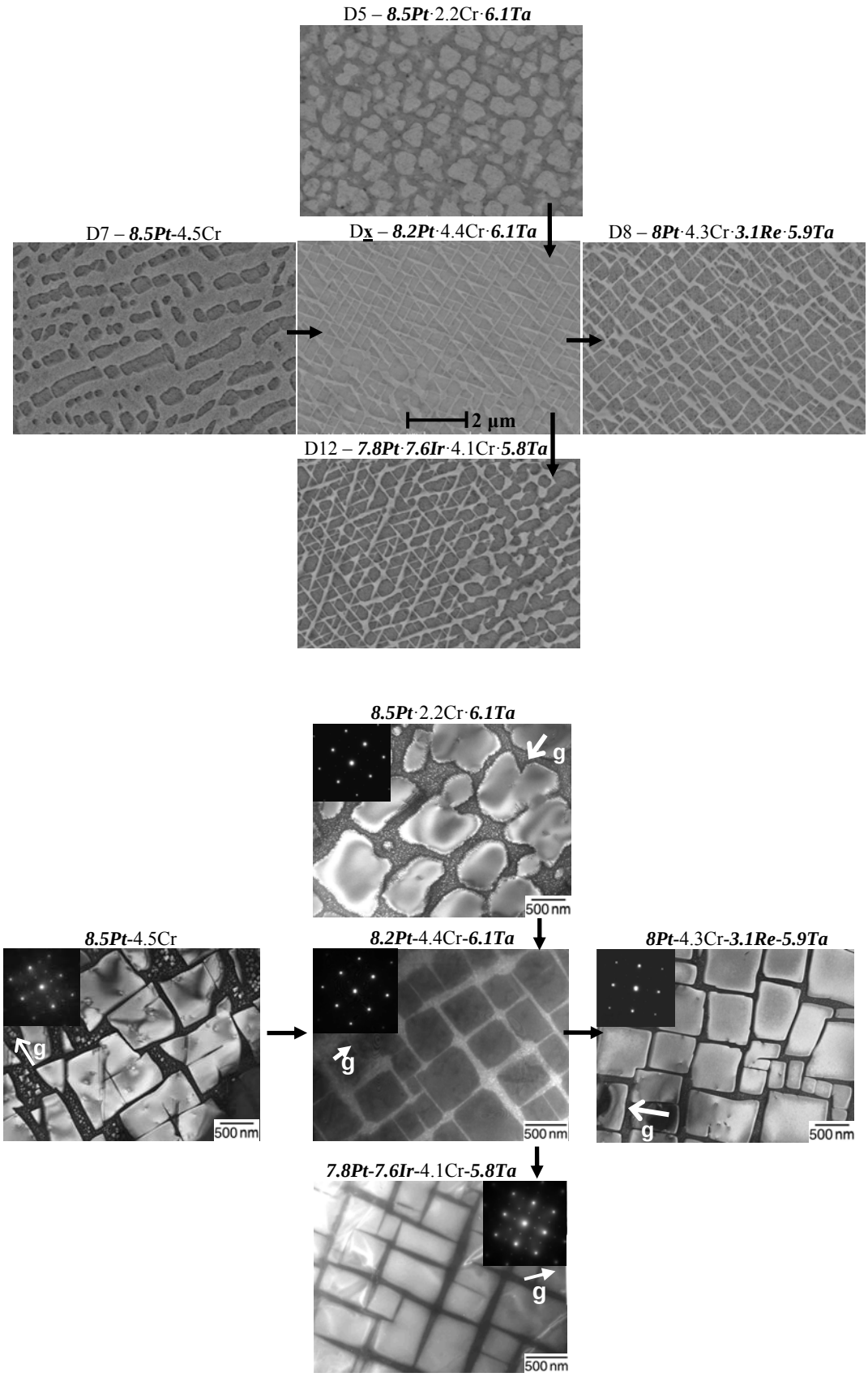

Figure 3: Changes in microstructure (Phase I) due to additions of various elements. All alloys contain (in wt%) (6.7-7)Al-0.3Hf. Alloy D**x** was used for microstructural studies only and was heat treated similarly to Phase I.

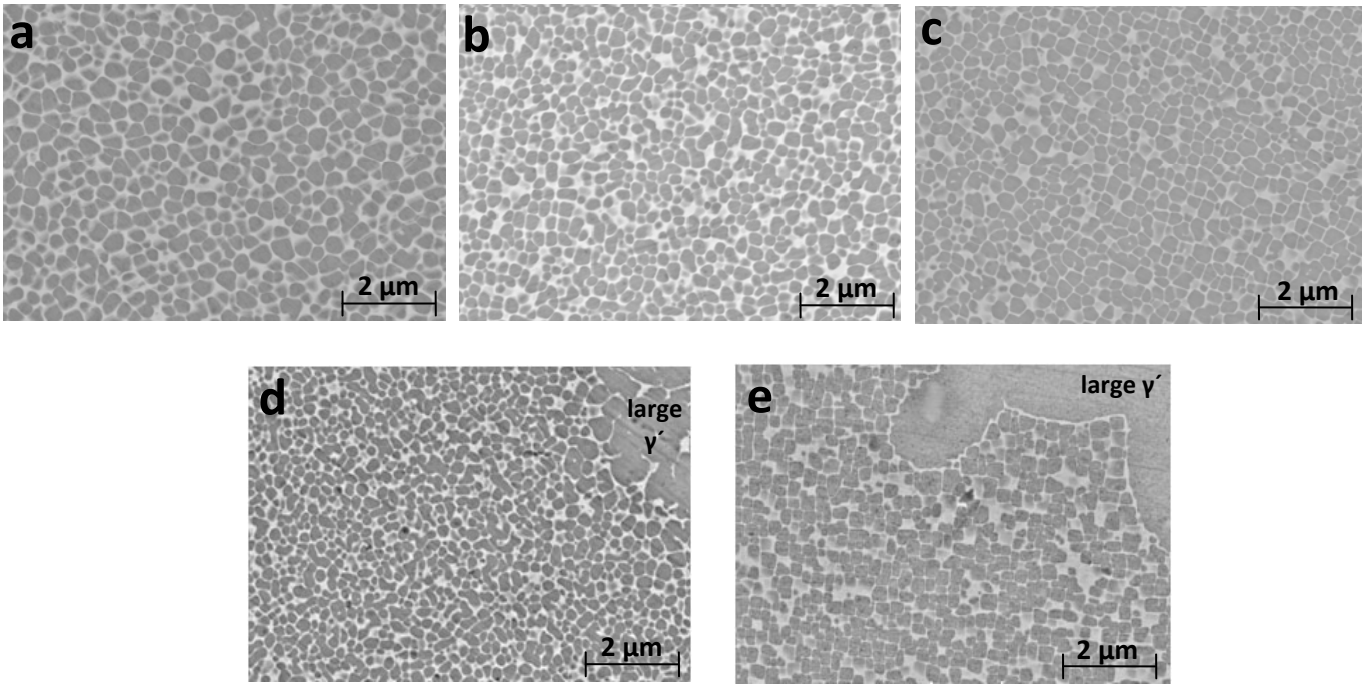

Figure 4: Microstructure of Phase II alloys as-aged. (a) - (e) represents alloys D19, D22, D24, D25, and D27, respectively.

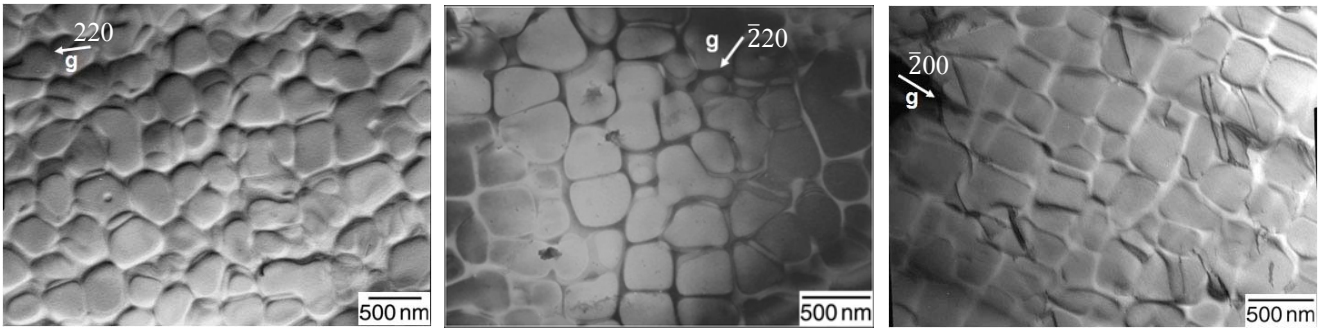

Figure 5: Microstructure of Phase II alloys. From left to right: D19, D22, and D27.
Images were taken off **B** = [001] axis.

have z-contrast differences arise due to etching effects as all samples in Figure 3 were imaged prior to etching with no appreciable z-contrast variation. Comparing alloys D7 and D<u>x</u> which differ in composition by 6.1 wt% Ta, this addition increases volume fraction of precipitates and results in a more cuboidal morphology. Adding Re to D<u>x</u> results in alloy D8, which has a fully cuboidal microstructure. Adding Cr from D5 to D<u>x</u> results in a cuboidal γ´ precipitates, with some degree of irregular morphology. Considering D<u>x</u> compared to D12, the Ir addition, does not change the morphology appreciably. From the TEM micrographs of Figure 3, additions of Ta and/or Cr result in cuboidal precipitate morphologies with well defined matrix channels. The strain energy in the Ir containing alloy is apparent with γ´ particle splitting observed in the particles. Additionally, from Figure 3 it is apparent that these alloys (and other alloys not shown here) have coherent γ - γ´ interfaces.

Figure 4 shows SEM micrographs of heat treated alloys from the Phase II matrix. Aside from D27, all other alloys display a semi-spherical morphology, which is indicative of near-zero precipitate-matrix misfit [25]. Alloys D25 and D27 retain large γ´ particles, ranging from 3 to 5 µm in diameter following solution treatment. These particles, which did not undergo dissolution up to a few degrees below the solidus, are consistent with the presence of the DTA peak at 1329°C, which was observed in Figure 2. Figure 5 shows TEM views of the microstructure of Phase II alloys after heat treatment. Precipitate morphologies range from semi-spherical to semi-cuboidal, as in alloys D19 and D22. Furthermore, isolated dislocations are apparent within some of the alloys, as shown for D27.

<u>Creep and Post-Creep Analysis</u>

Table II lists alloys crept at 1000°C in compression. Alloys are designated either by Phase I or Phase II and are further grouped by their respective PGM additions. Phase I alloys, aside from D3, all have minimum creep rates of the same order magnitude of 10^{-8} s^{-1}. In this regard, creep strengths can be estimated by the

Table II. Compression Creep Table of Phase I and II PGM alloys

Phase I All alloys contain (in wt%):Ni-(6.3-7.0)Al-0.3Hf									
PGM Additions	Composition						Stress MPa / (ksi)	Creep Rate (s^{-1})	Total Time to 1% (Hrs.)
	Alloy	Pt	Ir	Cr	Re	Ta			
Ir	D1	0	8.1	2.2	0	6.1	55 / 8.0	$1.3 \cdot 10^{-8}$	168.1
	D3	0	8.4	4.6	0	0	60 / 8.7	$1.3 \cdot 10^{-7}$	21.5
	D4	0	7.9	4.3	3.1	6	55 / 8.0	$5.6 \cdot 10^{-8}$	58.4
Pt	D5	8.2	0	2.2	0	6.1	80 / 11.6	$1.6 \cdot 10^{-8}$	80.2
	D7	8.5	0	4.5	0	0	80 / 11.6	$5.5 \cdot 10^{-8}$	32.5
	D8	8	0	4.3	3.1	5.9	100 / 14.5	RUPTURE	
Ir-Pt	D10	7.6	7.5	2	2.9	5.6	55 / 8.0	$7.9 \cdot 10^{-8}$	47.5
	D12	7.8	7.6	4.1	0	5.8	70 / 10.2	$1.2 \cdot 10^{-8}$	196.1
	D13	7.9	7.8	4.2	3	0	65 / 9.4	$6.0 \cdot 10^{-8}$	63.3
Higher Pt	D15	15.1	0	2	2.9	5.6	60 / 8.7	$6.2 \cdot 10^{-8}$	58.7
	D17	15.5	0	4.1	0	5.7	60 / 8.7	$4.4 \cdot 10^{-8}$	69.3
	D18	15.8	0	4.2	3	0	50 / 7.3	$5.6 \cdot 10^{-8}$	230
Phase II **All alloys contain (in wt%): Ni-(6-6.5)Al-(3.8-4.2)Cr-(2.8-3.2)Re-(5.3-5.8)Ta-0.3Hf**									
	Composition						Stress MPa /ksi	Creep Rate (s^{-1})	Total Time to 1% (Hrs.)
	Alloy	Pt	Ir	Ru	W				
Pt	D19	7.8	0	1.6	2.9		80 / 11.6	RUPTURE	
	D22	7.6	0	3.1	5.7		65 / 9.4	$3.8 \cdot 10^{-8}$	103.3
Ir-Pt	D24	7.4	5.8	1.5	5.6		75 / 10.9	$1.4 \cdot 10^{-7}$	28.5
	D25	7.5	5.9	3.1	2.8		70 / 10.2	$3.4 \cdot 10^{-8}$	79.3
Higher Pt	D27	14.8	0	1.5	2.8		55 / 8.0	$5.7 \cdot 10^{-8}$	41.7

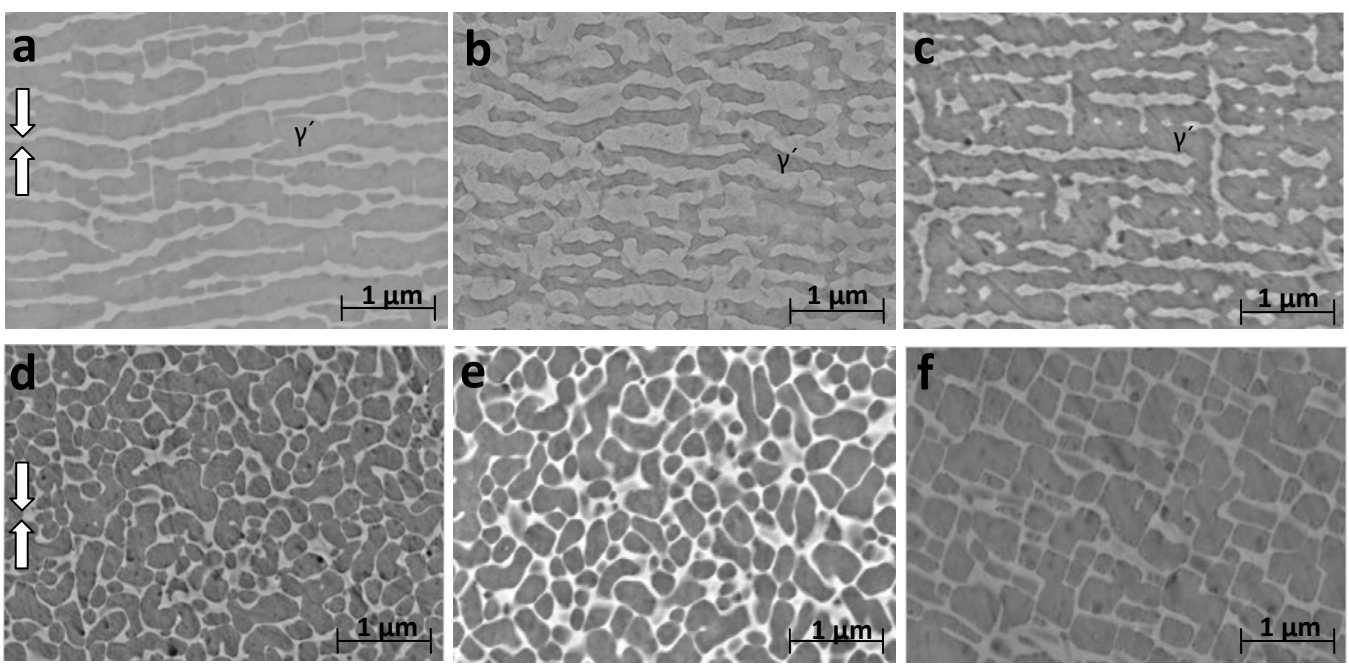

Figure 6: Directional coarsening of various Phase I (a - c) and II (d - f) alloys. The white arrows indicate the direction of applied stress. All micrographs were imaged parallel to the applied stress axis. (a) – (c) represent alloys D4, D10, and D12, and (d) – (f) are D22, D24, and D27, respectively.

comparison of the magnitudes of the applied stresses needed to establish this creep rate. Alloys containing only Ir were the weakest, whereas alloys containing only Pt exhibited the highest creep strengths. A combination of Ir and Pt gave creep resistances slightly higher than the Ir-only alloys but not as high as the Pt-only PGM alloys. The Phase II alloys exhibit creep rates of the order of 10^{-8} s^{-1}, aside from D24. Considering the similar creep rates, D25 sustained the highest stress while D22 followed. Comparing Phase I and Phase II alloys, PGM alloys containing both Ir and Pt gave high overall creep resistance while alloys containing Pt in excess of 14 wt% showed lower creep strengths regardless of other alloying additions.

Figure 6 shows the directional coarsening behavior for Phase I and II alloys. The white arrows indicate the direction of the applied compressive stress. In alloys D4, D10, and D12, precipitates elongated transverse to the stress axis. The γ′ in these alloys displays dark contrast compared to the bright contrast of the matrix. The elongation of the γ′ normal to the applied compressive stress axis is indicative of positive misfit behavior. Some precipitates in these alloys are not perfectly aligned parallel to the stress axis due to their polycrystalline structure with equiaxed grains not aligned along the <001> direction. Overall, all alloys from the four PGM groups in Phase I displayed rafting consistent with positive misfit. Here, misfit is defined as:

$$\delta = 2\ x\ \frac{a_{\gamma'} - a_{\gamma}}{a_{\gamma'} + a_{\gamma}} \qquad \text{Eq.2}$$

where a_{γ} and $a_{\gamma'}$ are the lattice parameters of the matrix and precipitate, respectively.

The additions of Ru and W to the Phase II alloys resulted in a different precipitate coarsening behavior. The bottom row of Figure 6 shows that the coarsened precipitates do not have a preferential orientation, without elongation either parallel or perpendicular to the stress axis. This type of behavior is neither positive nor negative but is representative of a misfit value that is close to zero. Near-zero misfit is consistent with the near-spherical precipitate morphologies for these alloys in the as heat-treated state.

Lattice Misfit Estimation

Figure 7 highlights some of the interfacial dislocations existing in post-creep specimens. Using Eq. (1), lattice misfits were estimated from these interfacial dislocation alloys from Phase I. Figure 7 (a) – (c) are Phase I alloys and (d) and (e) are Phase II alloys. The estimated lattice misfits (positive) for alloys D3, D5, and D17 were 0.24, 1.0 and 0.94%, respectively. Overall, alloys containing only Ir displayed magnitudes ranging from 0.2 - 0.35% whereas alloys with higher Pt had higher misfit, ranging from 0.9 - 1.5%. PGM alloys with Ir and Pt averaged around 0.3 - 0.6% and alloys containing Pt at lower levels were 0.45 - 1.3%. High temperature synchrotron X-ray experiments on selected alloys confirm positive misfit at high temperature [33]. Misfit estimations for Phase II alloys could not be ascertained, even though coarsening occurred, due to low densities and irregularly distributed dislocations. In addition, dislocations within the precipitates were not as pronounced in Phase II alloys as they were within the Phase I group.

Discussion

Precipitate Morphology and Directional Coarsening

The microstructure and directional coarsening of PGM-containing superalloys is sensitive to the type of PGM addition and its influence on partitioning of other elements in the system. The unusual feature of the Pt and Ir-containing superalloys studied here is the existence of a positive precipitate-matrix misfit, unlike alloys with Ru additions [25, 26]. In the Pt-containing alloys studied here the positive misfit occurs due to the strong partitioning of the Pt to the γ′ phase. However, given the range of precipitate morphologies observed, Figure 3, it is clear that the partitioning is also influenced by other alloying additions. For example, Cr and/or Ta additions can change the morphology of γ′ phase towards cuboidal, shown in Figure 3. Since Ta is known to preferentially partition to the $L1_2$ [2, 34], then it is likely that higher Cr additions partition Pt to a higher extent into the matrix. Ir does not have a dramatic effect on precipitate morphology since this element partitions near equally between both phases, as shown by comparison of the microstructure of Dx to D12.

Directional coarsening, also known as 'rafting', occurs at high temperatures under an applied uniaxial stress [35-37]. During compression tests, 'negative' type rafting behavior is associated with the coalescence of the precipitates parallel to the stress axis while 'positive' type behavior is normal to the axis. All Phase I alloys investigated displayed positive type rafting behavior as seen in the SEM images of Figure 6. This again, is due to Pt preferentially partitioning to the precipitate, thereby increasing the $a_{\gamma'}$ lattice parameter. The higher Pt containing alloys from Phase I would have higher γ′ lattice parameters which are greater than those containing the lesser amounts of Pt. This increase in the magnitude of the misfit, observed in Figure 7 for Phase I, results in closely spaced dislocations at the γ - γ′ interface. Alloys that contain Ir or Ir and Pt still exhibit positive type rafting behavior due to strong partitioning of platinum and tantalum, with the presence of Ir.

While Ru and W typically partition more equally between both phases [15, 38], the spherical nature of the particles in Phase II alloys may suggest that Ru and W are partitioning with the presence of the PGM elements to a higher extent to the matrix, reducing the misfit from strongly positive to near-zero. It has been observed earlier [15] that the partitioning of Ir was influenced by elements such as Ru and W, which can result in increased Ir in the precipitate. Atom probe experiments similar to those of Tin *et al.* [38, 39] would clearly be useful for further elucidation of partitioning in these PGM alloys. SEM images of Figures 4 and 5 indicate that additions of Ru and W have increased a_{γ}, implying that a reasonable amount of these elements are in the γ matrix. Although magnitudes could not be verified through TEM, coarsening was observed in all Phase II samples with no preferential direction. Since this is indicative of near-zero misfit, this could potentially be a problem for high temperature creep deformation since the gamma particles do not coalesce uniformly to form rafts, leaving vertical and horizontal matrix channels open for dislocations to glide during creep.

Creep Properties

Alloys containing low Pt or a combination of Ir and Pt demonstrated the highest creep strengths. Although the high Pt alloys displayed misfit magnitudes of about 1.0%, they were the least resistant to creep deformation. Even though alloys

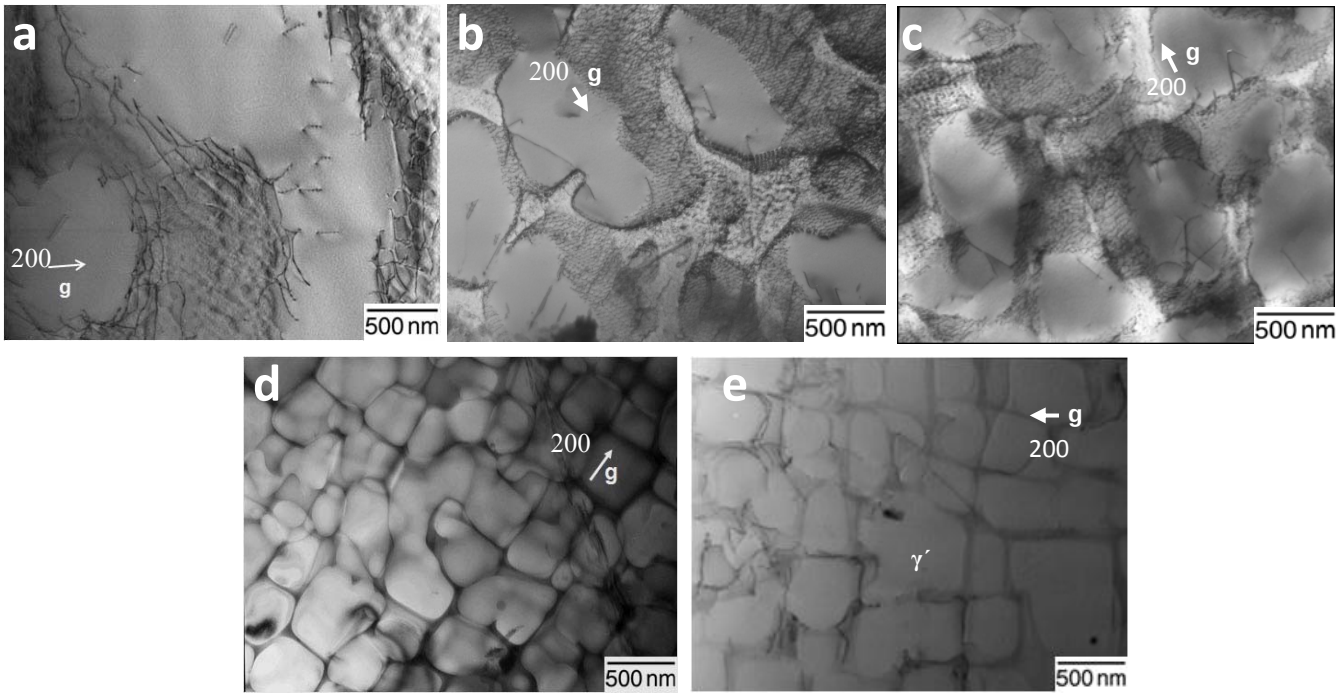

Figure 7: γ - γ´ interfacial dislocations for lattice misfit estimation on Phase I and II alloys. Alloys (a)-(c) are D3, D5, and D17. Images (d) and (e) are D22 and D24. Images were taken off the **B** = [001] zone axis.

containing Ir displayed misfit values around 0.3%, Ir is apparently not effective as a creep-strengthening element and stresses greater than 60 MPa were not sustained. From Table II, comparing D1 to D5, where the only difference is the PGM addition, demonstrates that Pt increases the creep resistance while Ir does not. This is unexpected since Ir interdiffusion in Ni is slow [40]. Further alloying with Ta improved creep resistance at high temperature which would be expected since Ta is known as a strengthening element for the $L1_2$. Direct comparison between D5 and D7 indicates that Ta helps reduce total strain accumulation over longer periods of time. Thus a likely explanation for the improvement in creep strength due to Ta is that this element increases the shearing resistance of the precipitates after coarsening has occurred, forcing dislocations to move only within the matrix. However, many samples from Phase I, including Ta-containing alloys, did contain dislocations within the precipitates following creep deformation. Further TEM analyses of the substructure following creep over a wider range of testing conditions would be useful.

Considering the creep properties of bond coat materials at temperatures around 1000°C, alloys investigated here show creep strengths that are nearly 40-50 MPa higher than typical bond coats composed of B2 NiAl-based or β-γ NiCrAlY materials [41-43]. (Ni,Pt)Al bond coats, crept at 1000°C at stresses near 80 MPa, displayed creep rates of the magnitude 10^{-4} s^{-1} with Pt additions in excess of 15 wt%. Interestingly, alloys investigated here that displayed the highest creep strengths contained at most 8 wt% Pt and 8 wt% Ir, which is considerably less than most Pt-modified bond coats.

Comparison of the PGM alloys studied here to commercial superalloys shows that the PGM alloys do not possess the same degree of creep resistance. Polycrystalline superalloy MAR-M247 can sustain a creep rate of 10^{-8} s^{-1} at 982°C at a stress of 172 MPa [44], while the alloys investigated here can tolerate approximately 80 MPa under the same creep conditions. However, many aspects of the present alloys have not been optimized, including solid solution strengthening of both phases, aging heat treatments and additions of grain boundary strengthening elements such as C and B. Thus, in their present form, the creep resistance of the PGM alloys is higher than presently available bond coats but lower than high refractory cast alloys.

Conclusions

Ni-base superalloys containing Pt and/or Ir have been investigated over a relatively wide range of compositions, with the following observations:

1.) Pt preferentially partitions to γ´, which can make misfit magnitudes greater than zero and up to 1.0%. The γ´ morphology varies considerably based with alloying elements added beyond Pt and Ir. Cr and Ta have a strong effect on precipitate morphology and partitioning. Ru and W lower misfit to near-zero, resulting in near-spherical precipitate morphologies.

2) Ta additions in Phase I alloys raise the γ´ solvus temperature close to the solidus mark, leaving a solution treatment window of about 20-50°C, depending on the level of PGM additions.

3) Alloys with a combination of Ir and Pt or only Pt possess the highest creep strengths. Creep strengths exceeded those of conventional bond coats but are lower than high refractory content superalloys at 1000°C.

4) Directional coarsening shows that Phase I alloys display positive type behavior. Higher Pt contents increase $a_{\gamma'}$ which increases misfit magnitude. Misfit magnitudes were near-zero for

Phase II alloys and SEM and TEM images showed coarsening with no preferential orientation of precipitates in relation to the applied compressive stress.

Acknowledgements

The authors would like to thank the assistance and useful discussions with B. Gleeson from the University of Pittsburgh, A. Heidloff and T. Izumi from Iowa State University, W. Brindley from Rolls Royce Corporation, and D. Hardwick, and P. Martin of AFRL. This project was sponsored under research grant #F015404 from AFRL through the Rolls Royce Corp.

References

1. M.F.Ashby, and D.R.H. Jones, *Engineering Materials 1, 2nd Edition* (Oxford, England: Butterworth-Heinemann, 1996), 198.

2. R.C. Reed, *The Superalloys Fundamentals and Applications* (Cambridge, England: Cambridge University Press, 2006), 283.

3. D.R. Clarke, and C.G. Levi, "Materials Design for the Next Generation Thermal Barrier Coatings," *Annual Review of Materials Research* 33 (2003), 383-417.

4. B. Gleeson, "Thermal Barrier Coatings for Aeroengine Applications," *Journal of Propulsion and Power*, 22 (2) (2006), 375-383.

5. N.M. Yanar, M.J. Stiger, G.H. Meier, and F.S. Pettit, "Processing Effects on the Failure of EBPVD TBCs on MCrAlY and Platinum Aluminide Bond Coats," *Superalloys 2000*, ed. T.M. Pollock, R.D. Kissinger, et al. (Warrendale, PA: The Minerals, Metals, & Minerals Society, 2000), 621-628.

6. V.K. Tolpygo and D.R. Clarke, "On the Rumpling Mechanism in Nickel-Aluminide Coatings Part I: An Experimental Assessment," *Acta Materialia* 52 (17) (2004) 5115-5127.

7. J.A. Nesbitt, B. Gleeson, D. Sordelet, and C.A. Barrett, "Pt and Hf Additions to NiAl Bond Coats and Their Effect on the Lifetime of Thermal Barrier Coatings," *Materials Science Forum Vols.* 426-432 (2003) 209-214.

8. B. Tryon, K.S. Murphy, J.Y. Yang, C.G. Levi, and T.M. Pollock, "Hybrid Intermetallic Ru/Pt-Modified Bond Coatings for Thermal Barrier Systems," *Surface and Coatings Technology* 202 (2007) 349-361.

9. B. Gleeson, W. Wang, S. Hayashi, and D. Sordelet, "Effects of Platinum on the Interdiffusion and Oxidation Behavior of Ni-Al-Based Alloys," *Materials Science Forum* 461-464 (2004) 213-222.

10. S. Hayashi, S.I. Ford, D.J. Young, D.J. Sordelet, M.F. Besser, and B. Gleeson, "α-NiPt(Al) and Phase Equilibria in the Ni-Al-Pt System at 1150°C," *Acta Materialia* 53 (2005) 3319-3328.

11. R.A. Ricks, A.J. Porter, and R.C. Ecob, "The Growth of Gamma Prime Precipitates in Nickel-Base Superalloys," *Acta Metallurgica* 31(1) (1983) 43-53.

12. J.L. Kamm and W.M. Milligan, "Phase Stability in $(Ni,Pt)_3Al$ Alloys," *Scripta Metallurgica* et *Materialia* 31 (11) (1994), 1461-1464.

13. P.J. Hill, N. Adams, T. Biggs, P. Ellis, J. Hohls, S.S. Taylor, and I.M. Wolff, "Platinum Alloys Based on $Pt\text{-}Pt_3Al$ for Ultra-High Temperature Use," *Materials Science and Engineering* A329-331 (2002) 295-304.

14. T. Yokokawa, M. Osawa, K. Nishida, T. Kobayashi, Y. Koizumi, and H. Harada, "Partitioning Behavior of Platinum Group Metals on the γ and γ′ Phases in Ni-Base Superalloys at High Temperatures," *Scripta Materialia* 49 (2003) 1041-1046.

15. H. Murakami, T. Honma, Y. Koizumi, and H. Harada, "Distribution of Platinum Group Metals in Ni-Base Single-Crystal Superalloys," *Superalloys 2000*, ed. T.M. Pollock, R.D. Kissinger, et al. (Warrendale, PA: The Minerals, Metals, & Materials Society, 2000), 747-756.

16. M. Fährmann, P. Fratzl, O. Paris, E. Fährmann, and W.C. Johnson, "Influence of Coherency Stress on Microstructural Evolution in Model Ni-Al-Mo Alloys," *Acta Metallurgica* et *Materialia* 43 (3) (1995) 1007-1022.

17. A.F. Giamei, and D.L. Anton, "Rhenium Additions to a Ni-Base Superalloy: Effects on Microstructure," *Metallurgical Transactions A* 16A (1985) 1997-2005.

18. AC Yeh, CMF Rae, and S. Tin, "High Temperature Creep of Ru-Bearing Ni-Base Single Crystal Superalloys," *Superalloys 2004*, ed. K.A. Green, T.M. Pollock, et al. (Warrendale, PA: The Minerals, Metals, & Materials Society, 2004), 677-685.

19. A. Sato, H. Haraka, Y. Yokokawa, T. Murakumo, Y. Koizumi, T. Kobayashi, and H. Imai, "The Effects of Ru on the Phase Stability of Fourth Generation Ni-Base Single Crystal Superalloys," *Scripta Materialia* 54 (9) (2006), 1679-1684.

20. S. Walston, A. Cetel, R. MacKay, K. O'Hara, D. Duhl, and R. Dreshfield, "Joint Development of a Fourth Generation Single Crystal Superalloy," *Superalloys 2004*, ed. K.A. Green, T.M. Pollock, et al. (Warrendale, PA: The Minerals, Metals, & Materials Society, 2004), 15-24.

21. J.X. Zhang, J.C. Wang, H. Harada, and Y. Koizumi, "The Effects of Lattice Misfit on the Dislocation Motion in Superalloys During High-Temperature Low Stress Creep," *Acta Materialia* 53 (17) (2005), 4623-4633.

22. F. Pyczak, B. Devrient, F.C. Neuner, and H. Mughrabi, "The Influence of Different Alloying Elements on the Development of the γ/γ′ Microstructure of Nickel-Base Superalloys During High Temperature Annealing and Deformation," *Acta Materialia* 53 (2005), 3879-3891.

23. Y. Koizumi, Z. Jianxin, T. Kobayashi, T. Yokokawa, H. Harada, Y. Aoki, and M. Arai, "Development of Next Generation Ni-Base Single Crystal Superalloys Containing Ruthenium, "*Journal of the Japan Institute of Metals* 67 (9) (2003), 468-471.

24. A.P. Ofori, C.J. Rossouw, and C.J. Humphreys, "Determining the Site Occupancy of Ru in the $L1_2$ Phase of a Ni-Base Superalloy Using ALCHEMI," *Acta Materialia* 53 (1) (2005), 97-110.

25. L.J. Rowland, Q. Feng, and T.M. Pollock, "Microstructural Stability and Creep of Ru-Containing Ni-Base Superalloys," *Superalloys 2004*, ed. K.A. Green, T.M. Pollock, et al. (Warrendale, PA: The Minerals, Metals, & Materials Society, 2004), 697-706.

26. L.J. Carroll, Q. Feng, J.F. Mansfield, and T.M. Pollock, "High Refractory, Low Misfit Ru-Containing Single-Crystal Superalloys," *Metallurgical Transactions A* 37A (2006), 2927-2938.

27. T. Kobayashi, H. Harada, M. Osawa, and A. Sato, "Creep Strengths of Ir-Containing 5th Generation SC Superalloys," *Journal of the Japan Institute of Metals* 69 (12) (2005) 1099-1103.

28. T. Kobayashi, Y. Koizumi, H. Murakami, *et al.*, National Research Institute for Metals, Ibakari (JP), U.S. Patent #6,494,971, (2002).

29. G.L. Selman, and R.J. Midgley, Johnson Matthey & Company, Limited, U.S. Patent #4,683,119, (1987).

30. Q. Feng, T.K. Nandy, S. Tin, and T.M. Pollock, "Solidification of High-Refractory Ruthenium-Containing Superalloys," *Acta Materialia*, 51 (2003) 269-284.

31. S. Tin, T.M. Pollock, and W. Murphy, "Stabilization of Thermosolutal Convective Instabilities in Ni-Based Single Crystal Superalloys: Carbon Additions and Freckle Formation," *Metallurgical & Materials Transactions A*, 32 (A) (2001), 1743-1753.

32. L.J. Rowland, "Creep and Microstructural Stability of Ruthenium-Containing Nickel-Base Single Crystal Superalloys" (Ph.D. thesis, University of Michigan, 2005), 55.

33. A. Heidloff, J.S. Van Sluytman, B. Gleeson, and T.M. Pollock, "Alloy Design and Characterization of PGM-Modified $\gamma + \gamma'$ Ni-Base Systems for Surface and Structural Stability Part II: Structural Stability," *Metallurgical and Materials Transactions A*, *Currently under review.*

34. P. Caron, T. Khan, "Evolution of Ni-Based Superalloys for Single Crystal Bas Turbine Blade Applications," *Aerospace Science Technology*, 3 (1999), 513-523.

35. M. Kamaraj, "Rafting in Single Crystal Nickel-Base Superalloys – An Overview," *Sādhanā*, 28 (Pts. 1 & 2) (2003), 115-128.

36. O. Paris, M. Fährmann, E. Fährmann, T.M. Pollock, and P. Fratzl, "Early Stages of Precipitate Rafting in a Single Crystal Ni-Al-Mo Model Alloy Investigated by Small-Angle X-Ray Scattering and TEM," *Acta Materialia*, 45 (3) (1997) 1085-1097.

37. T.M. Pollock and A.S. Argon, "Directional Coarsening in Nickel-Base Single Crystals with High Volume Fractions in Coherent Precipitates," *Acta Metallurgica* et *Materialia*, 42 (6) (1994) 1859-1874.

38. R.C. Reed, A.C. Yeh, S. Tin, S.S. Babu, and M.K. Miller, "Identification of the Partitioning Characteristics of Ruthenium in Single Crystal Superalloys Using Atom Probe Tomography," *Scripta Materialia*, 51 (4) (2004), 327-331.

39. S. Tin, L. Zhang, A.P. Ofori, and M.K. Miller, "Atomic Partitioning of Platinum and Ruthenium in Advanced Single Crystal Ni-Based Superalloys," *Materials Science Forum*, 546-49 (3) (2007), 1187-1194.

40. M.S.A. Karunaratne, and R.C. Reed, "Interdiffusion of the Platinum-Group Metals in Nickel at Elevated Temperatures," *Acta Materialia*, 51 (10) (2003), 2905-2919.

41. D. Pan, M.W. Chen, P.K. Wright, and K.J. Hemker, "Evolution of a Diffusion Aluminide Bond Coat for Thermal Barrier Coatings During Thermal Cycling," *Acta Materialia*, 51 (8) (2003), 2205-2217.

42. L. Ajdelsztajn, D. Hulbert, A. Mukherjee, and M.J. Schoenung, "Creep Deformation Mechanism of Cryomilled NiCrAlY Bond Coat Material," *Surface Coatings and Technology*, 201 (2007), 9462-9467.

43. M.P. Taylor, H.E. Evans, E.P. Busso, and Z.Q. Qian, "Creep Properties of Pt-Aluminide Coating," *Acta Materialia*, 54 (2006), 3241-3252.

44. M.V. Nathal, R.D. Maier, and L.J. Ebert, "The Influence of Cobalt on the Tensile and Stress Rupture Properties of the Nickel-Base Superalloy MAR-M247," *Metallurgical Transactions A*, 13 (A) (1982), 1767-1774.